Earth and Planetary Science Letters 578 (2022) 117326

Contents lists available at ScienceDirect

Earth and Planetary Science Letters

www.elsevier.com/locate/epsl

# Impact of Late Pleistocene climate variability on paleo-erosion rates in the western Himalaya

Saptarshi Dey [a,*], Bodo Bookhagen [b], Rasmus C. Thiede [c], Hella Wittmann [d], Naveen Chauhan [e], Vikrant Jain [a], Manfred R. Strecker [b]

[a] Earth Science Discipline, Indian Institute of Technology Gandhinagar, Gujarat-382055, India
[b] Institute of Earth Sciences, University of Potsdam, Potsdam-14476, Germany
[c] Institute of Geosciences, Christian Albrechts University of Kiel, Kiel-24118, Germany
[d] Deutsches Geoforschungszentrum Potsdam, Potsdam-14473, Germany
[e] Physical Research Laboratory Ahmedabad, Gujarat-380009, India

ARTICLE INFO

*Article history:*
Received 19 June 2021
Received in revised form 18 November 2021
Accepted 26 November 2021
Available online xxxx
Editor: J.-P. Avouac

*Keywords:*
erosion
cosmogenic nuclides
luminescence dating
Indian summer monsoon
Himalaya

ABSTRACT

It has been proposed that at short timescales of $10^2$–$10^5$ yr, climatic variability can explain variations in sediment flux, but in orogens with pronounced climatic gradients rate changes caused by the oscillating efficiency in rainfall, runoff, and/or sediment transport and deposition are still not well-constrained. To explore landscape responses under variable climatic forcing, we evaluate time windows of prevailing sediment aggradation and related paleo-erosion rates from the southern flanks of the Dhauladhar Range in the western Himalaya. We compare past and present $^{10}$Be-derived erosion rates of well-dated Late Pleistocene fluvial landforms and modern river sediments and reconstruct the sediment aggradation and incision history based on new luminescence data. Our results document significant variations in erosion rates ranging from 0.1 to 3.4 mm/yr over the Late Pleistocene. We find that, during times of weak monsoon intensity, the moderately steep areas (hillslope angles of 27 ± 13°) erode at lower rates of 0.1–0.4 mm/yr compared to steeper (>40°) crestal regions of the Dhauladhar Range that erode at 0.8−1.3 mm/yr. In contrast, during several millennia of stronger monsoon intensity, both the moderately steep and high slope areas record higher erosion rates (>1-3.4 mm/yr). Lithological clast-count analysis shows that this increase of erosion is focused in the moderately steep areas, where Lesser Himalayan rocks are exposed. Our data thus highlight the highly non-linear response of climatic forcing on landscape evolution and suggest complex depositional processes and sedimentary signals in downstream areas.


## 1. Introduction

Magnitude of and changes in erosion rates in tectonically active orogens have been interpreted to result from various combinations of tectonic and climatic forcing, but the unambiguous attribution to specific forcing mechanisms has remained a major challenge (e.g., Armitage et al., 2011; Adams et al., 2020). Current understanding of these complex relationships suggests a dominant tectonic control on erosional flux over million-year timescales (e.g., DeCelles et al., 2001; Bonnet et al., 2007; Thiede et al., 2017), while fluctuations in sediment flux over timescales of $10^2$ to $10^5$ yr are commonly linked to the effects of climate change and episodes of climatic variability (e.g., Goodbred and Kuehl, 2000; Clift et al., 2008; Bookhagen et al., 2005; Bookhagen and Strecker, 2012; Tofelde et al., 2017; Mandal et al., 2021). In this study, we refer to erosion when discussing denudation rates derived from *in-situ* cosmogenic nuclide analysis and imply rates that integrate over timescales that involve *in-situ* production and production during transport processes, as well as chemical and physical weathering processes.

With respect to the Himalaya, erosion rates have been analyzed extensively using various methods and on timescales ranging from decades to millions of years (e.g., Wulf et al., 2010; Lupker et al., 2012; Lenard et al., 2020), often with differing results. For example, decadal-scale sediment gauging has identified erosion rates that average ca. 1 mm/yr, reflecting changes in monsoon-driven precipitation and runoff (e.g., Wulf et al., 2010). Similarly, on millennial timescales spanning the Late Pleistocene and Holocene, erosion and sediment transport appear to be associated with frequent intensified monsoonal periods, thus suggesting a close relationship between climatic forcing and mass transfer (Bookhagen et al., 2005; Clift et al., 2008; Scherler et al., 2015).

* Corresponding author.
*E-mail address:* saptarshi.dey@iitgn.ac.in (S. Dey).

https://doi.org/10.1016/j.epsl.2021.117326
0012-821X/

However, catchment-wide erosion rates derived from *in-situ* $^{10}$Be concentrations in Himalayan river sediments that span centuries to millennia with varying glacial conditions are difficult to link to a single erosion process and have thus been attributed to both tectonic and climatic forcing mechanisms (e.g., Vance et al., 2003; Lupker et al., 2012; Scherler et al., 2015). Similarly, on million-year timescales, erosion and exhumation rates ranging from <0.5 to >3 mm/yr have been obtained by low-temperature thermochronology studies (Thiede and Ehlers, 2013 and references therein; Blythe et al., 2007; Thiede et al., 2017). In these studies, variations in process rates have been linked to a combination of influences exerted by the geometry and activity of fault-bounded sectors of the orogen and superposed climate-driven processes (Adams et al., 2020; Thiede et al., 2017; Burbank et al., 2003).

In a recent study using *in-situ* cosmogenic $^{10}$Be measurements on offshore sediment cores from the Ganga-Brahmaputra system, Lenard et al. (2020) proposed that the erosional effects of late Cenozoic climatic changes were virtually undetectable in the retrieved sedimentary signals, suggesting a tectonically-driven, steady erosion rate of ∼1.1 mm/yr over the last 6 Myr. Conversely, investigations combining the effects of topographic steepness, rainfall, and vegetation cover on erosion have shown millennial-scale variations in sediment flux in the Himalayan orogen between ∼0.1 and 4 mm/yr (e.g., Olen et al., 2016; Adams et al., 2020). In addition, catchment-wide erosion studies in the Himalaya covering the Late Pleistocene were shown to be two to four times greater compared to those of today, thus indicating the influence of glacial cycles on erosion processes (Scherler et al., 2015). In addition, Kapannusch et al. (2020) suggested that low *in-situ* $^{10}$Be concentrations in fluvial terrace deposits possibly result from higher sub-glacial sediment input; they proposed that Late Pleistocene aggradation in the Yamuna River valley was mainly driven by reduced discharge, whereas higher erosion rates had a minor effect.

Taken together, these findings, although contradictory, are central to the ongoing debates about the influence of climate change on surface processes. In light of these environmental impacts associated with global climate change and to better understand the role of past and potential future fluctuations in the surface-process regime there is a need to search for reliable, co-genetic proxies of erosion in geomorphic records and geological archives. Although studies in different environments have succeeded in linking sediment-flux variability to climate fluctuations over millennial timescales (e.g., Demenocal et al., 2000; Bookhagen et al., 2005; Scherler et al., 2015; Dey et al., 2016; Garcin et al., 2017), it is not yet fully understood how to decipher the relative effects of combined tectonic and climatic forcing on these timescales, nor how different tectonically active sectors of the mountain belts (i.e., catchments) individually respond to climatic impacts. Likely, the highly dynamic nature of landscapes together with low preservation potential of landforms and sedimentary deposits has significantly hampered our ability to reconstruct sedimentary processes on timescales beyond the Last Glacial Maximum (LGM).

Precipitation, vegetation cover, and temperature constitute three of the most critical parameters for understanding paleoclimatic conditions and their potential impact on erosion and sedimentation (e.g., Olen et al., 2016). In the Himalayan realm, for example, monsoonal rainfall and glacial melting prompted by increased temperatures have been shown to cause higher discharge (e.g., Weldeab et al., 2019) that induces lateral scouring and failure of hillslopes (Bookhagen et al., 2005; Scherler et al., 2015), which ultimately leads to higher sediment yields in rivers (Wulf et al., 2010; Scherler et al., 2015). Whereas these relationships have been well-defined for shorter timescales, terrestrial cosmogenic nuclide measurements on quartz-rich sand from fluvial terrace sediments have made it possible to expand observations into the past and link hillslope erosion with past climatic changes exceeding decadal and centennial timescales (e.g., Charreau et al., 2011; Scherler et al., 2015; Kapannusch et al., 2020).

The uppermost coarse-clastic strata of multiple fluvial terraces carved into thick sediment fills in intermontane basins are particularly well suited to record climate-controlled variations in sediment transfer and are often used to study paleoclimatic and tectonic impacts on sedimentary and geomorphic processes (e.g., Bridgland and Westaway, 2008; Wegmann and Pazzaglia, 2009; Tofelde et al., 2017; Repasch et al., 2017). Such terrace sequences also exist in the Kangra Basin of the northwestern Himalaya. The Kangra Basin is an intermontane, tectonically controlled basin characterized by transient sediment storage in the form of different levels of fluvial and alluvial terrace deposits that mirror past oscillations in erosion, fluvial transport capacity, deposition, and thalweg abandonment. These terrace sediments are chronologically constrained (Srivastava et al., 2009; Thakur et al., 2014; Dey et al., 2016), with additional new age constraints on key sediment horizons presented below. Two different sequences of alluvial-fill deposits (AF1 and AF2) form terraces with a staircase morphology of increasingly younger terrace surfaces at decreasing elevation above the present-day thalweg. In addition, the tectonic, rock-uplift and long-term erosional framework of the sediment-source region, the Dhauladhar Range to the north, is well-documented (Deeken et al., 2011; Thiede et al., 2017). By combining an analysis of the geomorphic characteristics of the basin with our new $^{10}$Be-derived paleo-erosion rates and new age constraints on the duration of aggradation processes from Late Pleistocene–Holocene terrace sediments in the Kangra Basin, we are able to show that the Dhauladhar Range eroded at a lower rate during weak monsoonal conditions. Conversely, during stronger monsoon phases at the transition from glacial to interglacial periods, sediment delivery from moderately steep sectors in the landscape was enhanced.

## 2. Geological background

The Kangra Basin lies in the Kangra recess in Himachal Pradesh, India (Fig. 1). The basin is bounded by the Dhauladhar Range in the north (peaks >5500 m asl) and the uplifted Siwalik strata in the south, and stores sediments derived from the southern flank of the Dhauladhar Range (Figs. 1 and 2). The basin is drained by three major tributaries of the Beas River: The Baner River, the Gaj River, and the Neogal River (Fig. 2). The southern flank of the Dhauladhar Range is delimited by the Palampur Thrust (PT), the Main Boundary Thrust (MBT), and the Early Miocene Main Central Thrust (MCT). The Lesser Himalaya between the MBT and the MCT consists of slate, mica schists, and quartzites (Fuchs, 1975; Steck, 2003; Thiede et al., 2017). The Higher Himalayan Crystalline Sequence in the MCT hanging wall consists of garnet-bearing, amphibolite-grade mica schists, while gneiss and Ordovician granites define the crests of the Dhauladhar Range. Low-temperature thermochronology studies combined with thermal modeling document that the Dhauladhar Range has been uplifting since >8 Myr and exhumes with mean rates of ∼1.2–2 mm/yr (Thiede et al., 2017). The pattern of the low-temperature thermochronology ages obtained from the Dhauladhar Range document a simple exhumation process, which is driven by a deep-seated thrust ramp on the MBT that emerges from the Main Himalayan Thrust (MHT). Therefore, any major tectonic changes in the sediment-source area and tectonically controlled drainage reorganization affecting regional erosion processes over the investigated Late Pleistocene and Holocene timescales are unlikely.

The sedimentary architecture and aggradation of the Kangra basin fill were studied in detail by Srivastava et al. (2009) and Thakur et al. (2014) and further investigated by Dey et al. (2016). Results from surface-exposure dating of the abandoned fluvial terraces mark the onset of fluvial re-incision and a lowering of the

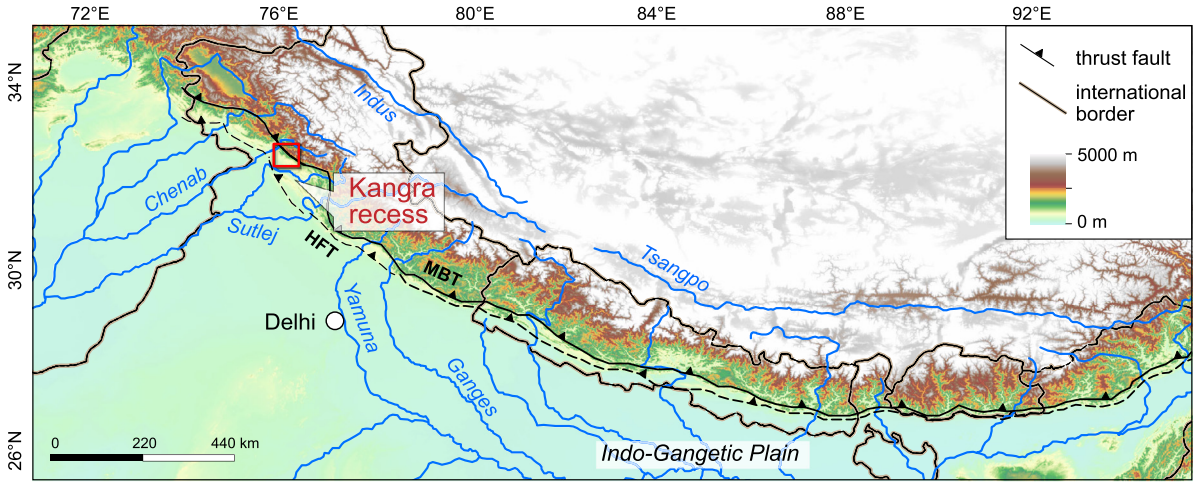


**Fig. 1.** Topographic map of the Himalaya showing two major tectonic boundaries of its southern edge (MBT and HFT) and important drainage systems. Our study area lies within the Kangra recess at the foot of the Dhauladhar Range (cf. extent of Fig. 2 is shown by red box). Abbreviations: MBT – Main Boundary Thrust, HFT – Himalayan Frontal Thrust. (For interpretation of the colors in the figure(s), the reader is referred to the web version of this article.)

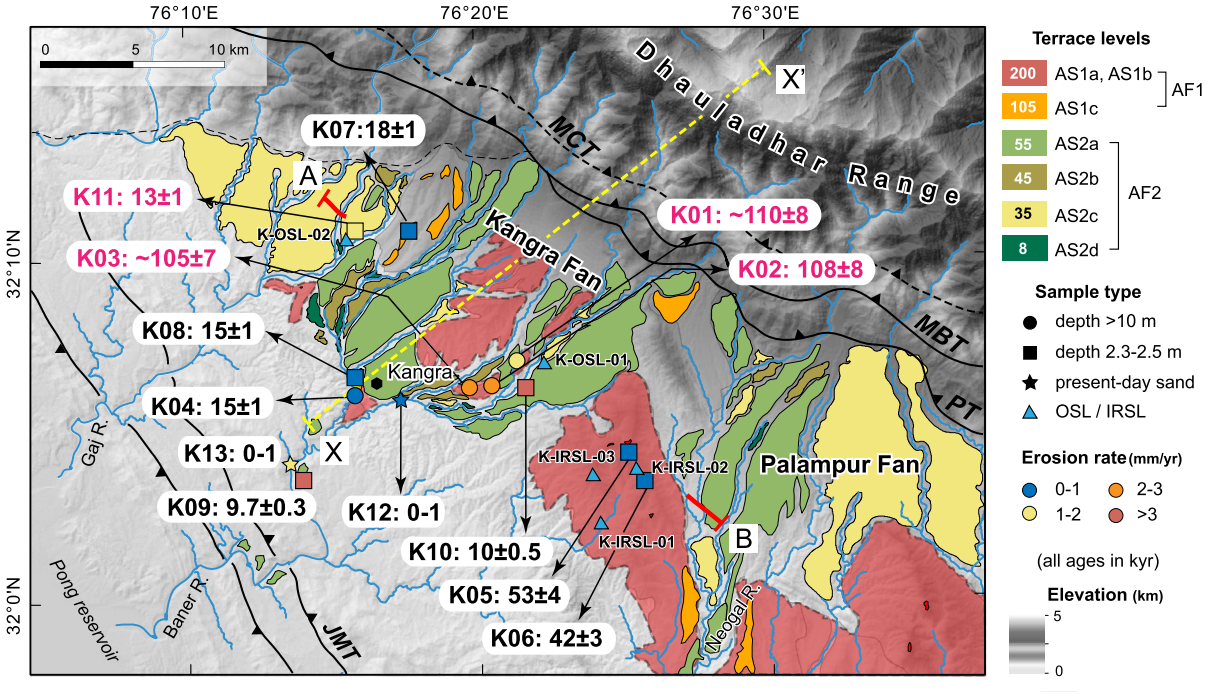


**Fig. 2.** Shaded topographic map of the study area showing the extent of preserved alluvial-fan sediments and fluvial terrace surfaces sculpted into them by recurrent fluvial incision and lowered base-level conditions. Interpreted depositional ages of samples based on $^{10}$Be exposure - age dating (Dey et al., 2016) and luminescence dating (Srivastava et al., 2009; Thakur et al., 2014) are shown. 4-km-wide topographic swath profile drawn along line X-X' is shown in Fig. 5b. Elevation profile along AB is shown in Fig. 3a. Quartz-clast-corrected, as well as floodplain-corrected, erosion rates from modern river sand and older sand layers preserved in fluvial terraces are shown. Abbreviation: AF – alluvial fan, PT – Palampur Thrust, JMT – Jwalamukhi Thrust, MCT – Main Central Thrust.

thalweg in the basin. The sediment archives in the basin have been classified into two major alluvial-fill (AF) phases, AF1 and AF2, which record the aggradation history since the penultimate Pleistocene warm period at ~130 kyr (Fig. 3a). AF1, the older aggradation phase, is associated with filling prior to the LGM (Dey et al., 2016). AF1 deposits correspond to a ~220–230-m-thick, poorly-sorted conglomeratic sequence dominated by quartzites derived from the Lesser Himalaya that reflects several aggradation phases, which were interrupted by phases of minor incision or non-deposition. The existence of well-defined, continuous paleosols is very limited. Srivastava et al. (2009) attempted to constrain the age of paleosol formation, but the age uncertainties do not allow stratigraphic correlation. At least three levels of well-preserved fluvial terraces have been sculpted into the AF1 fill (Dey et al., 2016). The top few meters of the terraces constitute a veneer of weathered fluvial gravels covering the rest of the AF1 fill (cf. Fig. 3e). Given their erosional nature and the thin veneer of conglomeratic gravel associated with transiently-stable base levels during the general trend of downcutting in the basin, we refer to these terrace levels as alluvial straths that reflect the abandonment of former thalwegs. The gravel-covered alluvial strath (AS) terraces AS1a, AS1b, and AS1c have thalweg-abandonment ages of 53 ± 3 kyr, 42 ± 2.7 kyr, and 18 ± 1.5 kyr, respectively (Fig. 3a) (Dey et al., 2016).

In contrast to the quartzite-dominated AF1 aggradation phase, the younger AF2 aggradation phase began after the LGM, and the

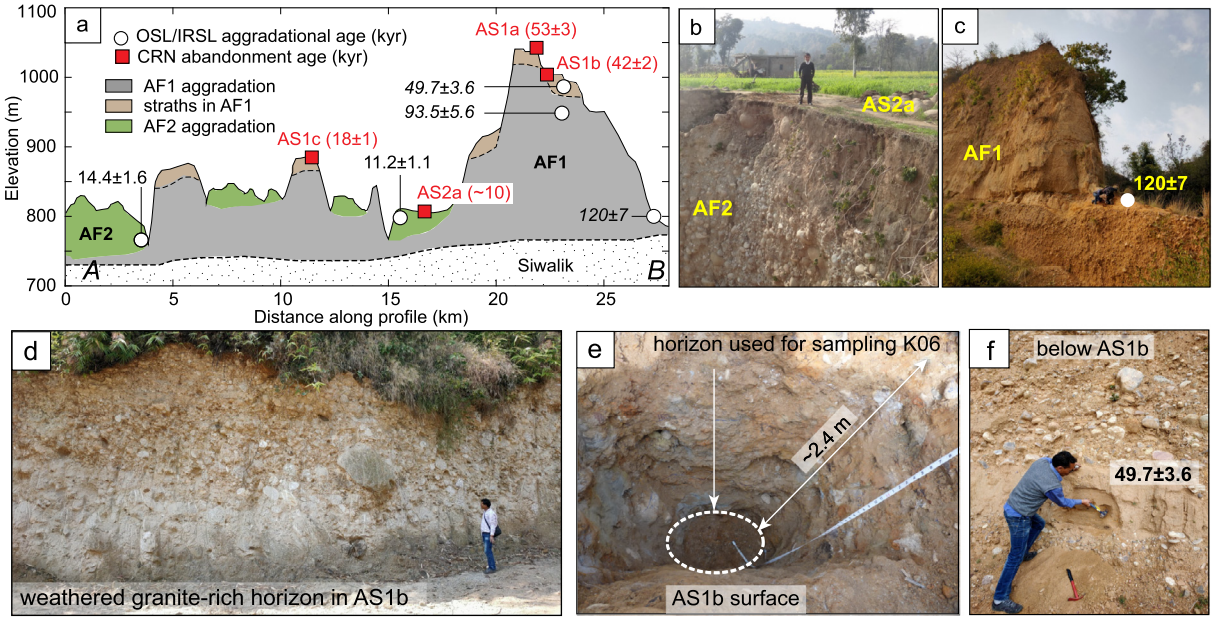


**Fig. 3.** (a) Schematic representation of sediment aggradation (AF1 and AF2) and re-incision phases (AS1a-AS1c and AS2a-AS2d) with corresponding depositional ages and terrace-abandonment ages (both in kyr) from Dey et al. (2016). The surface-profile location is shown in Fig. 2. (b) Field photograph of granite-rich AF2 fill unit beneath the AS2a surface. (c) Sampling horizon at the base of the AF1 fill near the village of Rajhoon. (d) Weathered horizon beneath AS2b. (e) Sampling site for K-IRSL-03 beneath AS2b surface. (e) Sampling pit for $^{10}$Be depth profile on AS2b. Sample K06 was taken from the bottom of the pit. (f) Sampling site for K-IRSL-03 beneath AS2b surface.

corresponding deposits are characterized by a pronounced increase in the abundance of granites from the Higher Himalaya, which are only exposed along the crest line of the Dhauladhar Range. Episodic re-incision of the AF2 fill is documented by four Holocene fluvial terrace levels: AS2a, AS2b, AS2c, and AS2d. In the nomenclature of Dey et al. (2016), these surfaces were previously labeled T3, T4, T5, and T6 (Supplementary Materials Fig. S1).

## 3. Methods

### 3.1. Processing steps for terrestrial cosmogenic radionuclide samples

We obtained 11 samples of amalgamated pebbles from buried sediment horizons of fluvial deposits in the Kangra Basin and two samples from a present-day river channel bar (Table 1), where we selectively sampled quartz-rich clasts of ~2-4 cm diameter (n > 25). These 13 samples were processed for measurements of in situ cosmogenic $^{10}$Be concentrations (Table 2; Fig. 2). Samples K01–K03 were taken from the base of the deposits that correspond to the AF1 aggradation phase, where the overlying sediment thickness is greater than 50 m. Sample K04 was taken from a depth of ~2.5 m below the AF1d aggradation unit, and samples K05–K11 were retrieved from the bottom of depth-profile pits (depth: 2.3–2.5 m below surface level) excavated on the terrace surfaces during an earlier study (Dey et al., 2016). Samples K05–K11 reported in this study are recalculated from published erosion-rate estimates (Dey et al., 2016) derived from the inherited $^{10}$Be concentration at the base of depth profiles. Methodological changes described in the following sections have resulted in changes in previously published erosion rates. Samples K12 and K13 are present-day river sediments taken from the Baner River near the town of Kangra and the village of Jalari, respectively (Fig. 2). Sample parameters are listed in Table 1.

The samples were chemically processed at the University of Potsdam and the German Research Center for Geosciences (GFZ) in Potsdam according to standard methods (e.g., von Blanckenburg, 2005). The $^{10}$Be measurements were carried out at the University of Cologne (relative to AMS standards KN01-6-2 and KN01-5-3) (Dewald et al., 2013) and at Lawrence Livermore National Laboratory (LLNL) (AMS standard 07KNSTD3110) that are consistent with a half-life of $^{10}$Be of 1.387 ± 0.012 My (Chmeleff et al., 2010). An average process blank $^{10}$Be/$^{9}$Be ratio of 2.2 × $10^{-16}$ (Cologne AMS) and 2.0 × $10^{-16}$ (LLNL AMS) was subtracted from the sample $^{10}$Be/$^{9}$Be ratios. All erosion rates calculated in this study employ the Lifton-Sato-Dunai (LSDn) model (Lifton et al., 2014) using the CRONUS-Earth online calculator (https://hess.ess.washington.edu/math/v3/v3_erosion_in.html) (Balco et al., 2008). We used a reference spallogenic production rate of 4.09 and atoms/y/g of quartz (Borchers et al., 2016) and a relative muonic production rate of 1.14% of the total production (Braucher et al., 2011). The concentrations of $^{10}$Be for all samples except the present-day river sands were corrected for post-burial $^{10}$Be accumulation (section 3.2). For catchment-wide production-rate estimation, we modified the commonly used approach based on hypsometry (e.g., Charreau et al., 2011). First, we assumed that past and present catchment boundary are the same. Secondly, we removed the area covered by the low-slope basin fill from the overall catchment based on a hillslope-angle filter with a lower cutoff of 10°. In this particular case, our approach did not yield any significant difference with respect to the commonly used standard-deviation based categorization of hillslope vs. low-gradient basin-fill areas (i.e., the floodplain correction of Wittmann et al., 2009). The floodplain correction results in a $^{10}$Be production rate representative for the sediment-producing area of the catchment, which is therefore higher than the basin-averaged production rate, because low-slope basin fill areas do not contribute significantly to the erosional flux (Wittmann et al., 2009). The average topographic shielding value of the remaining floodplain-corrected catchment was obtained using a pixel-by-pixel-based shielding correction in Topotoolbox (Schwanghart and Scherler, 2014). Note that we have not performed corrections of $^{10}$Be production rates due to glacial coverage, because the present-day glacial cover and the valley morphology of the crestal regions of the southern flank of the Dhauladhar Range suggest minimal glacial cover at present as well as during the Late Pleistocene. Catchment-wide erosion rates including all corresponding corrections (see below) are listed in Table 2.

**Table 1**
Details of sample locations, AMS measurements and site-specific production rates of samples from Kangra Basin.

| Sample details | | | | | | | | | | Catchment data (floodplain-corrected) | | AMS data | |
|---|---|---|---|---|---|---|---|---|---|---|---|---|---|
| Sample | Terrace level | Latitude (°) | Longitude (°) | Sample elevation (m) | Catchment-averaged ksn value ($m^{0.9}$)[a] | Age (kyr) | Depth from surface (cm) | Depth shielding factor | Site-specific production rate (atoms/gxyr) | Topographic shielding factor | Floodplain-corrected mean production rate (atoms/gxyr) | $[^{10}Be]_{measured}$ (atoms/g)[b] | $[^{10}Be]_{error}$ (atoms/g) |
| K01* | base of AF1 | 32.132 | 76.377 | 790 | 462 | 110 ± 8 | >5000 | 0 | 6.1 | 0.95 | 21.45 | 7521 | 348 |
| K02* | base of AF1 | 32.126 | 76.372 | 795 | 409 | 108 ± 8 | >5000 | 0 | 6.12 | 0.95 | 21.45 | 2490 | 265 |
| K03* | base of AF1 | 32.114 | 76.356 | 795 | 408 | 105 ± 7 | >5000 | 0 | 6.12 | 0.95 | 21.45 | 3483 | 119 |
| K04* | T2 | 32.106 | 76.262 | 750 | 230 | 18 ± 1.5 | 250 | 0.04 | 6.23 | 0.95 | 21.45 | 50208 | 1564 |
| K05 | T1-P1 | 32.068 | 76.399 | 1125 | 283 | 53 ± 4 | 220 | 0.06 | 8.22 | 0.95 | 21.45 | 115407 | 5159 |
| K06 | T1-P2 | 32.059 | 76.426 | 1120 | 280 | 42 ± 2.7 | 240 | 0.05 | 8.19 | 0.95 | 21.45 | 43714 | 1937 |
| K07 | T2-P1 | 32.184 | 76.297 | 1015 | 397 | 18 ± 1.5 | 250 | 0.04 | 7.61 | 0.96 | 17.43 | 32396 | 818 |
| K08 | T2-P2 | 32.106 | 76.262 | 750 | 231 | 15.5 ± 1.2 | 230 | 0.06 | 6.23 | 0.95 | 21.45 | 29100 | 1090 |
| K09 | T3-P1 | 32.058 | 76.227 | 625 | 233 | 9.5 ± 0.7 | 250 | 0.04 | 5.66 | 0.95 | 21.45 | 6332 | 554 |
| K10 | T3-P2 | 32.098 | 76.344 | 760 | 455 | 10.3 ± 0.8 | 240 | 0.05 | 6.27 | 0.95 | 21.45 | 6597 | 544 |
| K11 | T5-P1 | 32.183 | 76.276 | 715 | 477 | 13 ± 0.5 | 250 | 0.04 | 6.07 | 0.96 | 17.43 | 7118 | 626 |
| K12* | T0 | 32.091 | 76.255 | 603 | 285 | 0-0.5 | 0 | 1 | 5.35 | 0.96 | 21.45 | 12026 | 971 |
| K13 | T0 | 32.058 | 76.227 | 535 | 232 | 0-0.5 | 0 | 1 | 5.01 | 0.95 | 21.45 | 7713 | 340 |

[a] Corrected for floodplain contribution, T0 – modern river sand.
[b] As derived from accelerator mass spectrometer (AMS) measurement; * - samples measured in Lawrence Livermore National Laboratory, USA.
Mean elevation of LH quartzite = 1925 m asl.
Mean elevation of HH granite = 3120 m asl.
Sample ages are adapted from Dey et al. (2016), Thakur et al. (2014). Ages of K01-K03 approximated from Srivastava et al. (2009) and one IRSL sample from AF1 sequence (details provided in Supplementary material Fig. S2).

**Table 2**
Details of $^{10}Be$ concentrations, corrections (shielding from burial, decay, floodplain-correction and quartz-content correction) and resulting corrected erosion rates following LSDn model (Lifton et al., 2014).

| Sample details | Post-depositional correction | | | | $^{10}Be$ concentration used in Cronus calculator to calculate floodplain-corrected erosion rates | | Floodplain-corrected erosion rate | | Quartz- content and clast-contribution correction | | | | | | Final corrected erosion rate | |
|---|---|---|---|---|---|---|---|---|---|---|---|---|---|---|---|---|
| Sample | $[^{10}Be]_{spallation}$ (atoms/g) | $[^{10}Be]_{muon}$ (atoms/g) | $[^{10}Be]_{accumulated}$ (atoms/g) | $[^{10}Be]_{decay}$ (atoms/g) | $[^{10}Be]_{erosion}$ (atoms/g) | $[^{10}Be]_{error}$ (atoms/g) | Erosion rate (mm/yr) | Erosion rate error (mm/yr) | $Quartz_{quartzite}$ (g) | $Quartz_{granite}$ (g) | $f_{HH}$ | $f_{LH}$ | Quartz contribution ratio HH:LH | $P_{clast}$ (atoms/g/y) | Quartz-clast corrected erosion rate (mm/yr) | Quartz-clast corrected erosion rate error (mm/yr) |
| K01* | 0 | 0 | 0 | 395 | 7916 | 348 | 1.34 | 0.16 | 735 | 221 | 0.23 | 0.77 | 0.30 | 16.57 | 1.1 | 0.12 |
| K02* | 0 | 0 | 0 | 131 | 2621 | 265 | 3.77 | 0.82 | 1183 | 213 | 0.15 | 0.85 | 0.18 | 15.57 | 2.9 | 0.63 |
| K03* | 0 | 0 | 0 | 184 | 3667 | 119 | 2.74 | 0.27 | 969 | 241 | 0.20 | 0.80 | 0.25 | 16.15 | 2.2 | 0.22 |
| K04* | 3987 | 2240 | 6227 | 507 | 44488 | 1564 | 0.25 | 0.018 | 1181 | 203 | 0.15 | 0.85 | 0.17 | 15.48 | 0.19 | 0.02 |
| K05 | 26140 | 8480 | 34620 | 3589 | 84376 | 5159 | 0.14 | 0.02 | 674 | 205 | 0.23 | 0.77 | 0.30 | 16.56 | 0.11 | 0.02 |
| K06 | 17199 | 6468 | 23667 | 892 | 20939 | 1937 | 0.53 | 0.072 | 1028 | 212 | 0.17 | 0.83 | 0.21 | 15.92 | 0.41 | 0.07 |
| K07 | 5480 | 2664 | 8144 | 327 | 24579 | 818 | 0.38 | 0.041 | 774 | 226 | 0.23 | 0.77 | 0.29 | 16.69 | 0.37 | 0.04 |
| K08 | 5981 | 2336 | 8317 | 294 | 21077 | 1090 | 0.52 | 0.063 | 1044 | 210 | 0.17 | 0.83 | 0.20 | 15.94 | 0.40 | 0.06 |
| K09 | 2173 | 1306 | 3479 | 62 | 2915 | 554 | 3.41 | 1.32 | 350 | 291 | 0.45 | 0.55 | 0.83 | 19.92 | 3.2 | 1.24 |
| K10 | 2727 | 1270 | 3998 | 67 | 2666 | 544 | 3.71 | 1.53 | 402 | 281 | 0.41 | 0.59 | 0.70 | 19.28 | 3.4 | 1.3 |
| K11 | 1311 | 907 | 2218 | 71 | 4971 | 626 | 1.76 | 0.46 | 441 | 270 | 0.38 | 0.62 | 0.61 | 18.83 | 1.9 | 0.48 |
| K12* | 0 | 0 | 0 | 0 | 12026 | 971 | 0.91 | 0.16 | 398 | 239 | 0.38 | 0.63 | 0.60 | 18.76 | 0.81 | 0.14 |
| K13 | 0 | 0 | 0 | 0 | 7713 | 340 | 1.4 | 0.18 | 303 | 253 | 0.45 | 0.55 | 0.84 | 19.63 | 1.3 | 0.15 |

**Table 3**
Details of luminescence samples from Kangra Basin. Central age model (CAM) has been used for age estimation (Bailey and Arnold, 2006).

| Sample name | Latitude (°) | Longitude (°) | Elevation from river-bed (m) | U (ppm) | Th (ppm) | K (%) | Dose rate (Gy/kyr) | Equivalent dose (De) (Gy) | OD (%) | Depositional age (kyr) |
|---|---|---|---|---|---|---|---|---|---|---|
| K-IRSL-01 | 32.04513 | 76.40918 | 15 | 3.3 ± 0.1 | 13.8 ± 0.1 | 2.21 ± 0.1 | 3.74 ± 0.11 | 451 ± 24 | 17 | 120.5 ± 7.1 |
| K-IRSL-02 | 32.06433 | 76.42612 | 165 | 3.5 ± 0.1 | 15.8 ± 0.1 | 2.30 ± 0.1 | 4.01 ± 0.10 | 375 ± 20 | 14 | 93.5 ± 5.6 |
| K-IRSL-03 | 32.06852 | 76.39611 | 185 | 3.2 ± 0.1 | 15.3 ± 0.1 | 2.52 ± 0.1 | 4.09 ± 0.12 | 204 ± 14 | 14 | 49.7 ± 3.6 |
| K-OSL-01 | 32.11488 | 76.36896 | 44 | 3.1 ± 0.1 | 9.5 ± 0.1 | 1.96 ± 0.1 | 3.22 ± 0.08 | 36.1 ± 4.1 | 18 | 11.2 ± 1.1 |
| K-OSL-02 | 32.19728 | 76.22509 | 12 | 3.8 ± 0.1 | 16.9 ± 0.1 | 1.98 ± 0.1 | 3.80 ± 0.08 | 55 ± 5.9 | 21 | 14.4 ± 1.6 |

a- Moisture content assumed 10 ± 2%.
b- IRSL ages are not corrected for fading.

### 3.2. Correction for post-burial changes in concentration of $^{10}Be$

Within the upper few meters of the Earth's surface, post-depositional accumulation of $^{10}$Be in any sample is mainly caused by neutron spallation. However, at greater depths of at least 10 m, fast muons and negative muon capture play a crucial role in $^{10}$Be accumulation (Dunai, 2010). The measured $^{10}$Be concentration ($[^{10}Be]_{measured}$, in at/g) therefore needs to be corrected for the post-burial accumulation of $^{10}$Be ($[^{10}Be]_{accumulated}$, in at/g) ($[^{10}Be]_{accumulated} = [^{10}Be]_{spallation} + [^{10}Be]_{muon}$) as well as for radioactive decay ($[^{10}Be]_{decayed}$, in at/g) to obtain the post-depositional and burial-corrected $[^{10}Be]_{erosion}$ (representing the $^{10}$Be concentration at the time of deposition, in at/g) based on the following equation:

$$[^{10}Be]_{erosion} = [^{10}Be]_{measured} + [^{10}Be]_{decayed} - [^{10}Be]_{accumulated} \quad (1)$$

Accordingly, samples collected at depths of ~2.3–2.5 m were corrected for $^{10}$Be accumulation from spallation, muon capture, and fast muons (Table 1). The depositional ages of the respective samples were used for correcting $^{10}$Be concentrations due to radioactive decay ($t_{1/2} = 1.387$ Myr for $^{10}$Be). For older samples (>100 kyr) taken at the base of the sediment bodies, we only calculated the post-depositional radioactive decay component, because the depth of burial is beyond any significant accumulation due to spallation and muon capture. The production rates due to spallation and muon capture were estimated using algorithms provided by Hidy et al. (2010).

Post-depositional corrections change the $^{10}$Be concentration used for erosion-rate calculation. Whereas corrected concentrations for sediments buried at a depth of >50 m (sample K01, K02, and K03) are estimated to be 5% higher than measured, samples from the bottom of the 2.3–2.5 m depth-profile pits are calculated to have up to 60% lower "post-deposition corrected" concentrations (Table 2).

### 3.3. Quartz contribution from the Lesser and Higher Himalaya

We recorded the respective weights of granites and quartzites for each sample, in the 250–500 μm size fractions prior to leaching with acids (Table 2). Abundances of free quartz in the Dhauladhar granite and the LH quartzites were measured by grain count (grain size ~250–500 μm) under the microscope. Average abundances of free quartz obtained from three samples, each from the Higher Himalayan (HH) granites and the Lesser Himalayan (LH) quartzites, are ~30% and ~70% respectively. Therefore, the quartz-contribution ratio ($quartz_{granite}$: $quartz_{quartzite}$ or, quartz contribution factor HH/LH) from different sources can be expressed as the ratio of quartz derived from quartzite ($quartz_{quartzite}$) versus quartz derived from granite ($quartz_{granite}$):

$$quartz_{quartzite} = w_{quartzite} \times 0.7 \quad (2)$$

$$quartz_{granite} = w_{granite} \times 0.3 \quad (3)$$

Therefore, the fractional contributions of HH ($f_{HH}$) versus LH ($f_{LH}$) can be calculated from:

$$f_{HH} = quartz_{granite}/(quartz_{granite} + quartz_{quartzite}) \quad (4)$$

$$f_{LH} = quartz_{quartzite}/(quartz_{granite} + quartz_{quartzite}) \quad (5)$$

The mean production rates of the area exposing quartzites and granites are different because they come from different morphotectonic domains of the Lesser Himalaya/Upper Siwalik and Higher Himalaya, respectively. The spatial extent of these two rock types is well-constrained (Steck, 2003; Dey et al., 2016). A production rate corrected for quartz content and clast contribution ($P_{clast}$), hereafter referred to as "quartz-content correction", was obtained by

$$P_{clast} = P_{granite} \times f_{HH} + P_{quartzite} \times f_{LH} \quad (6)$$

where, $P_{granite}$ provides the mean production rate per area covered by granite and $P_{quartzite}$ represents the mean production rate of an area covered by quartzite (Table 1).

### 3.4. Luminescence dating

Luminescence dating, despite expected complex exposure histories in mountainous terrain, has been used in dating fluvial, glacial, lacustrine, and aeolian sediments (e.g., Thompson et al., 2018). The most common complexity arises from either heterogeneous bleaching of transported sediments (Srivastava and Misra, 2012) or poor luminescence sensitivity (Jaiswal et al., 2008), but for fluvial sediments that have traveled ~30–40 km from their sources, these two factors are insignificant.

We sampled key horizons from the AF1 and AF2 fill (as described in section 2) to better constrain the timing of sediment aggradation in the Kangra Basin; see Figs. 2 and 3 for location and stratigraphic setting. Sample K-IRSL-01 was taken from the base of the gently-tilted (~5° towards NE) AF1 unit near the village Rajhoon. Samples K-IRSL-02 and K-IRSL-03 were taken from near the top of the AF1 fill, but below the strath surfaces AS1a and AS1b, respectively. Samples K-OSL-01 and K-OSL-02 were taken from the top and the base of the early Holocene AF2 fill.

Samples from the AF1 unit were first measured with the OSL Single Aliquot Regenerative (SAR) method (Murray and Wintle, 2003), which generated a saturated signal. The post-IR infrared (pIR-IR) technique was also applied, but the sensitivity issues persisted. We relied on IRSL dating (Preusser, 2003) knowing that there is a possibility of signal fading in older samples. We did not correct for signal fading, and the IRSL ages are interpreted as minimum ages. OSL dating for the AF2 sediments relied on the OSL double-SAR protocol to filter feldspar contamination arising from granitic sources of the sediment (Roberts, 2007). A detailed sample processing and analytical protocol are documented in Appendix B, analytical outputs are shown in Supplementary Fig. S2 and additional sample information is provided in Table 3.

## 4. Results

### 4.1. Paleo-erosion rates and present-day erosion rates from cosmogenic $^{10}Be$

Paleo-erosion rates obtained from Equation (1) (corrected for post-depositional accumulation, decay, and floodplain area) exhibit a large range from 0.14 ± 0.02 to 3.8 ± 1.5 mm/yr (Table 1) over the last ∼120 kyr. These paleo-erosion rates were further corrected using $P_{clast}$ following Equation (6) (see Table 2). After the quartz-clast correction that normalizes the quartz content, we observe an overall reduction in erosion-rate estimates by about 10–20%, resulting in a range of 0.11 ± 0.02 to 3.4 ± 1.3 mm/yr. In this study we report and use the quartz-content corrected erosion rates.

The present-day river samples yield centennial to millennial-scale catchment-wide erosion rates of 0.8 ± 0.1 mm/yr (K12) and 1.3 ± 0.2 mm/yr (K13), respectively. After quartz-clast correction, samples K02 and K03 from the base of the AF1 fill yield erosion rates of 2.9 ± 0.6 mm/yr and 2.2 ± 0.2 mm/yr, respectively. Similarly, high erosion rates of 3.2 ± 1.2 mm/yr, 3.4 ± 1.3 mm/yr, and 1.9 ± 0.5 mm/yr are derived from samples K09, K10, and K11 of the deposits of the AF2 aggradation phase (∼14–9 kyr). The remaining samples (AS1a–AS1c) yield paleo-erosion rates of ≤0.4 mm/yr. In short, we observe two narrow time windows between ∼110 and 100 kyr and between ∼15 and 10 kyr that were characterized by substantially higher erosion (>1 mm/yr), whereas most of the remainder of our data show erosion rates of ≤0.4 mm/yr for the area of the Dhauladhar Range.

### 4.2. Luminescence dating

The new IRSL dating of the K-IRSL-01, K-IRSL-02, and K-IRSL-03 samples from the AF1 unit yielded minimum depositional ages of 120.5 ± 7.1 kyr, 93.5 ± 5.6 kyr, and 49.7 ± 3.6 kyr, respectively (Table 3). OSL dating of the K-OSL-01 and K-OSL-02 of the AF2 unit yielded depositional ages of 11.2 ± 1.1 kyr and 14.4 ± 1.6 kyr, respectively (Table 3). With these new data we are able to significantly improve temporal constraints of the timing of aggradation of both AF1 and AF2, compared to previously available data.

## 5. Discussion

Our results suggest that in the Kangra Basin sediment transport rates and sediment source areas have varied significantly over the last ∼120–130 kyr, whereas the tectonic boundary conditions have remained the same during the Late Quaternary. In order to explore the influence of climatic variations on erosional and depositional processes in this tectonically active area, we compared our $^{10}$Be-derived paleo-erosion rates with regional climatic and tectono-morphometric proxies.

### 5.1. Sediment aggradation and re-incision in the Kangra Basin

In combination with our previous work on the timing on terrace abandonment in the Kangra Basin (Dey et al., 2016), the new luminescence ages from our study provide additional information about major aggradation and re-incision events in the Kangra Basin (Fig. 4a). We are able to show that aggradation in the basin occurred in at least two principal phases: AF1 (120 ± 7–93 ± 5 kyr) and AF2 (∼15–10 kyr) (Fig. 4a). However, we cannot rule out that net aggradation in the basin of up to ∼100 m may have continued until ∼50 kyr (Fig. 3a). Constraining the complete aggradation and re-incision history of the basin is difficult due to multiple fill-and-cut cycles and a general low preservation potential leading to weak age control. We acknowledge that part of the sediment record may be missing. Nonetheless, based on the limited preservation of the fills in form of conglomeratic surface remnants at high elevations and their reconstructed regional extent, we are able to constrain a tentative record of re-incision highlighted by the ages of the abandonment of thalwegs and the formation of strath terraces at ∼59–50 kyr (AS1a), ∼45–40 kyr (AS1b), ∼22–16 kyr (AS1c), and ∼10 kyr–present (AS2a-AS2d), respectively (Fig. 4a). Although geochronological uncertainties and limited data do not allow us to draw unambiguous conclusions about potential linkages between terrace formation and monsoonal variability, we observe an overall trend towards aggradation during periods with high monsoonal variability between 90–120 kyr and 16–10 kyr (Fig. 4a). Conversely, thalweg incision and abandonment of strath surfaces correlates with periods of reduced variability and declining strength of the Indian Summer Monsoon (ISM). This correlation is in general agreement with our previous findings (Bookhagen et al., 2005; Dey et al., 2016). Notably, during the period between ∼80 and 16 kyr (except during 60–53 kyr), the ISM was comparatively weaker than during the last millennia (Cheng et al., 2016, cf. Fig. 4b), and there may have been several other re-incision phases that are not recorded. The rate of sediment filling during the initial stages of AF1 are higher (5.6 ± 0.5 mm/yr) than during the later stage (1.6 ± 0.2 mm/yr) (Fig. 4a), which is in line with a decrease in the ISM intensity at ∼80–60 kyr (Fig. 4b). Any sediment record of large-scale sediment removal prior to ∼60 kyr is not preserved. During 60–53 kyr, monsoon intensity increased and could have triggered sediment aggradation in the basin. The vertical terrace incision rates during AS1a–AS1c and AS2a–AS2d are within a similar range (∼3–4 mm/yr). Only during the ∼18–16 kyr dry period are the incision rates significantly higher (∼20 mm/yr). In general, our results are in accordance with those from earlier studies in the Himalaya that link aggradation with protracted periods of greater moisture availability and runoff (Pratt et al., 2002; Bookhagen et al., 2005).

### 5.2. Considerations of erosion-rate calculations

Samples procured from aggraded Late Pleistocene to Holocene sedimentary units exhibit large variations in $^{10}$Be concentrations (Table 1) and thus indicate a wide range of paleo-erosion rates from ∼0.1 to 3.4 mm/yr (Table 2). Measured concentrations were treated for post-depositional $^{10}$Be accumulation as well as floodplain correction in order to reduce or eliminate the bias caused by overestimation from $^{10}$Be inheritance. We assume that the main sources of $^{10}$Be inheritance are remobilization of sediments derived from low-relief areas and transiently stored fluvial deposits from low-slope areas exposed to cosmic rays. Conversely, sediments sourced along the steep hillslopes of the Dhauladhar Range, where no transient storage of sediments is observed, should have no or only very low inheritance.

Furthermore, we have taken into account the quartz-content correction, a weight-based correction of quartz contribution from different lithological units in the measured samples (section 3.3). Because the quartz-content correction is based on clast counts and the relative abundance of free quartz in each processed sample, the quartz-content correction may introduce a methodological bias. However, the overall signal prevails even without propagation of these corrections into paleo-erosion rate estimates: low erosion rates during incision phases AS1a–AS1c vs. high erosion rates during the aggradation of AF1 and AF2 (Table 2). We thus conclude that the wide range of $^{10}$Be concentrations is geologically sound and is not affected by a correction bias.

### 5.3. Increased erosion rates during times of stronger monsoons

Fluctuations in oxygen-isotope ratios ($\delta^{18}$O) derived from cave speleothems typically document variability in climatic oscillations

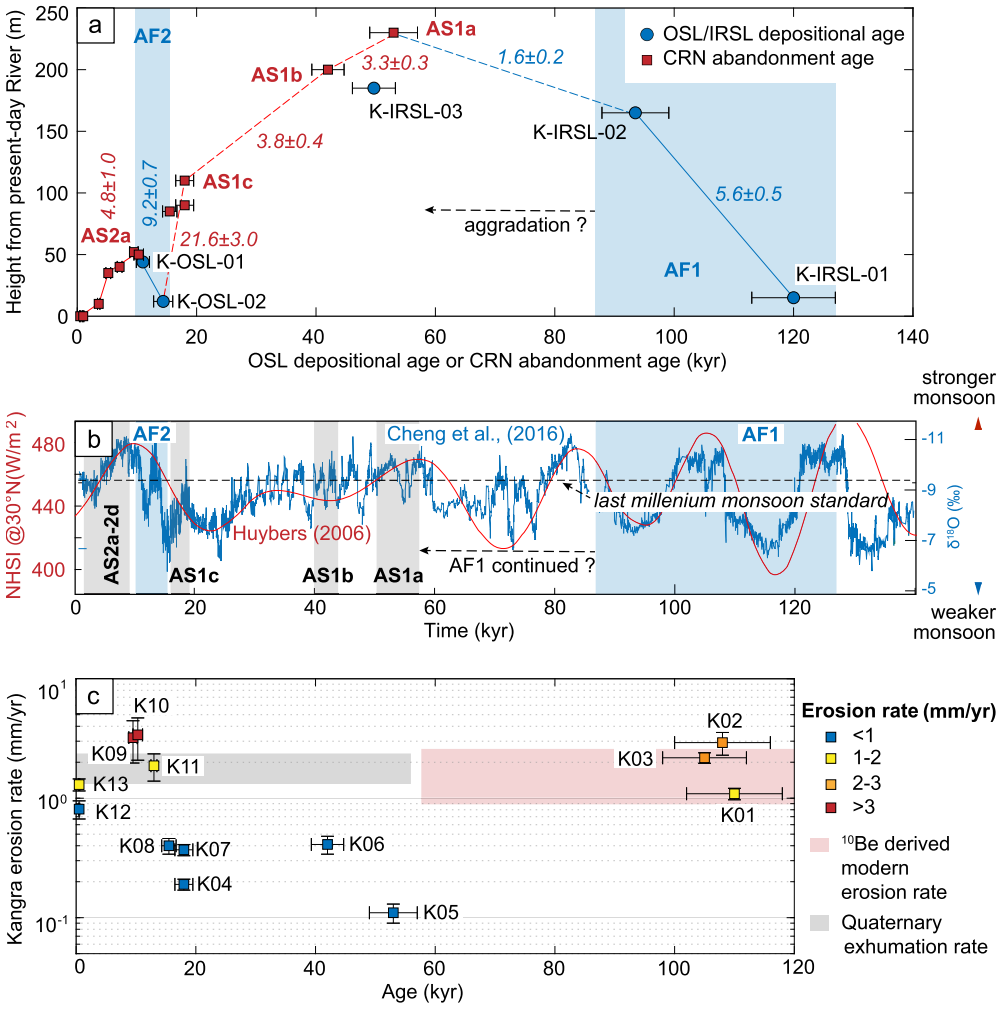


**Fig. 4.** (a) $^{10}$Be-based terrace abandonment ages ($\pm 1\sigma$ uncertainties) (Dey et al., 2016) and OSL/IRSL depositional ages from Kangra Basin with corresponding sediment-filling rates (blue) and sediment-removal rates (red). (b) Oxygen-isotope records from Sanbao caves in China (Cheng et al., 2016) and Northern Hemisphere summer solar insolation (NHSI) data at 30°N (Huybers, 2006) show linkages between changes of continental climate trends. Sediment aggradation in the basin correlates with phases of a stronger, wetter ISM, while sediment-evacuation phases correlate with declining ISM periods or weaker ISM periods compared to the last millennium. (c) Distribution of erosion rates obtained from sediments from the Kangra Basin over time. Late Pleistocene–Holocene erosion rates are slower than the exhumation rate at million-year timescales (Thiede et al., 2017). High erosion rates temporally correlate with periods of strong summer monsoon activity and increasing orbital precession, while the comparatively weaker summer monsoon phases exhibit lower erosion rates.

at glacial timescales. In the greater Indian realm, the patterns of $\delta^{18}$O data have been interpreted to reflect oscillations in summer-monsoon cycles on $10^3$- to $10^4$-yr timescales (Fig. 4b). Compiled $\delta^{18}$O measurements from the Sanbao caves in China (Cheng et al., 2016) provide high-resolution moisture proxy records over the entire period of interest (Fig. 4b). We use these as a proxy for variations of ISM strength. As a temperature proxy, we use solar insolation at 30°N for the months of June to August (Huybers, 2006). Our luminescence samples and cosmogenic nuclide erosion-rate samples were taken from basin fill and the conglomeratic veneer of strath terraces. These terraces reflect depositional and incision processes, which we attribute to changes in monsoonal strength (Fig. 4), as summarized above.

Samples obtained from the base of the AF1 and AF2 phases yield high erosion rates of >1.9 mm/yr (Fig. 4c). Whereas dating uncertainties preclude us from making clear correlations, a comparison of the timing with oxygen-isotope records suggests that AF1 and AF2 were generated during periods of greater moisture availability or during the transition from drier glacial to more humid interglacial stages (Fig. 4b). Conversely, the samples associated with strath formation are characterized by low erosion rates (≤0.4 mm/yr) (Fig. 4c), and the phases of strath formation correlate with times of weaker monsoonal strength compared to the present day (Fig. 4b). $^{10}$Be-derived catchment-wide erosion rates estimated from modern river-sand samples (K12 and K13) from the Baner River yield erosion rates of 0.8–1.3 mm/yr, which are similar to the lower limit of $^{10}$Be-derived modern-day erosion rates (1.6 ± 0.8 mm/yr) measured at the foot of the central Dhauladhar Range (Godard et al., 2018). Combining these two data sets, we infer the $^{10}$Be-derived modern-day erosion rate of the Dhauladhar Range to be 1.4 ± 0.7 mm/yr, which is in agreement with modern erosion rates (~1.3 mm/yr) obtained from trans-Himalayan river basins (Lupker et al., 2012) and the Sutlej Valley to the east (Olen et al., 2016). Overall, there are distinctly different erosion rates recorded in the Kangra basin during stronger (>1.9 mm/yr) and weaker monsoon phases (≤0.4 mm/yr).

Modern-day erosion rates (1.4 ± 0.7 mm/yr) are at the lower range of the Myr-scale timescale exhumation rates (~1.2–2 mm/yr) obtained from the central part of the Dhauladhar Range (Thiede et al., 2017). However, the transiently higher paleo-erosion rates during wet phases balance this mismatch. Interestingly, major changes in exhumation are not observed over the past few Myr (Deeken et al., 2011) and thus suggest that the combination of lower and

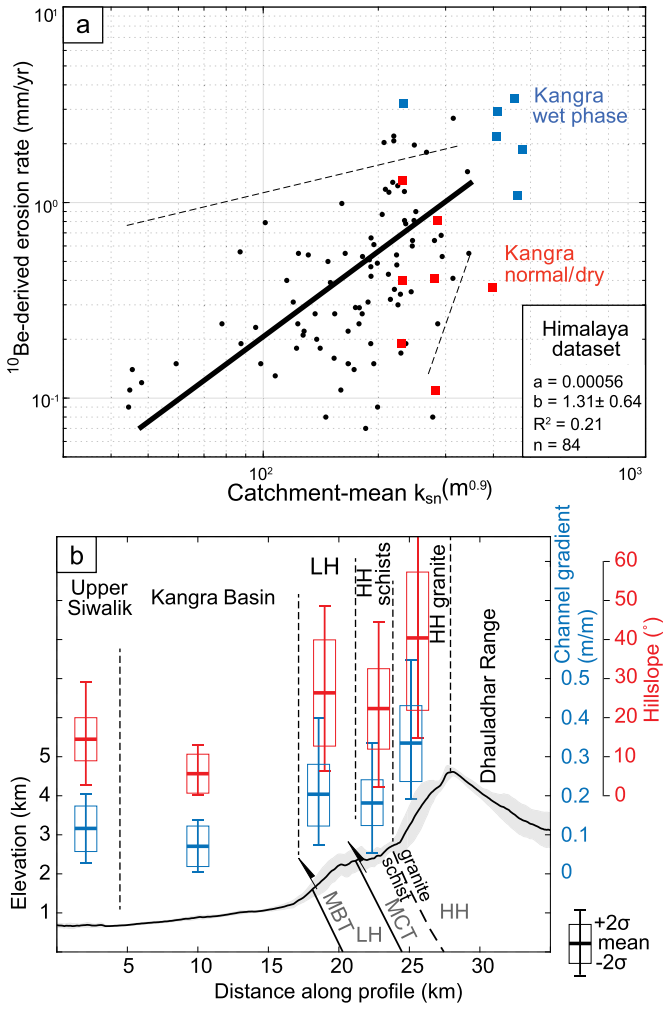


**Fig. 5.** (a) Power-law relationship between $^{10}$Be-derived catchment-mean erosion rates using modern river sand for individual drainage systems in the western and central Himalaya and mean channel steepness ($k_{sn}$) (Godard et al., 2014; Scherler et al., 2015; Olen et al., 2015) (in black). Paleo-erosion rates (quartz-clast and floodplain corrected) in Kangra Basin from wetter periods (blue) and drier periods (red) are also plotted with respective $k_{sn}$ values (catchment-averaged normalized steepness index). Note that published millennial-scale erosion rates from the Himalaya were not corrected for floodplain area and the erosion rates are calculated using the Lm age model (Lal, 1991; Stone, 2000). Regression fitting shows best fit (solid line) and 95% confidence interval (dashed lines). The values are equally weighted and the paleo-erosion data from Kangra are not included in the regression fit. (b) Pattern of change in elevation within a swath-window of 4 km drawn along line X-X' (cf. Fig. 2). The gray-shaded region defines the elevation range and the solid black line defines the mean elevation across the swath window. Hillslope angle and channel gradient of different lithologic or morphotectonic domains are shown as boxplots defining the mean, $2\sigma$ and the range. These relationships illustrate the characteristic differences in erosional efficiency between the steep Higher Himalaya and the moderately steep Lesser Himalaya.

higher erosion rates of the past ~120 kyr lead to comparable erosion rates derived from apatite-fission track thermochronology.

### 5.4. Topographic steepness vs. paleo-erosion rates and evaluation of tectonic controls

Comparing erosion rates from different geographic and morphotectonic areas in an orogen is difficult because the gravitational force that controls erosion varies with the slope of the terrain. In order to normalize erosion-rate measurements and to allow comparison between different areas, we use the parameter of landscape steepness (Kirby and Whipple, 2012; Lague, 2014). Previous studies (e.g., Olen et al., 2016; Adams et al., 2020) have shown a power-law relationship between catchment-averaged steepness index and erosion rate, where steeper landscapes usually erode faster. To investigate these relationships further, we compiled an erosion-rate data set from the Western Himalaya (Olen et al., 2016 and references therein) and compared it to our results obtained from both wetter and drier monsoon periods (Fig. 5a). The dry phases with monsoonal conditions similar to that of the present day correspond closely to the modern erosion rates from the Western Himalaya observed for a given steepness index. However, for the same steepness index, the erosion rates during enhanced, wetter monsoon phases are significantly higher than any modern erosion rates measured (Fig. 5a). Thus, although topographic steepness dictates the efficiency of erosion in general, this finding is evidence that erosion rates are significantly modulated by the influence of climatic forcing.

To distinguish between the steep and the moderately steep areas of the Dhauladhar Range, we measured the hillslope and channel gradients across the entire range and the Kangra Basin (Fig. 5b). The hillslope- and channel-gradient maps and a map showing the different lithologies are in the Supplementary Material (Figs. S3–S4). The crest of the Dhauladhar Range is occupied by granites and has steep channel gradients (0.3 ± 0.1 m/m) and steep hillslopes (40 ± 14°) (Fig. 5b). In contrast, the bedrock in the Lesser Himalaya comprises quartzite and mica-schists and exhibits moderate channel gradients (0.20 ± 0.08 m/m) as well as moderate hillslope values (27 ± 13°). The catchments exposing the Higher Himalayan schists are also characterized by moderate channel gradients (0.17 ± 0.07 m/m) and hillslope angles (23 ± 9°), similar to the Lesser Himalaya. Thus, the morphology of the Higher Himalayan granite domain is much steeper compared to the regions of the Higher Himalayan schists and the Lesser Himalaya and to the exposures of the Sub-Himalayan units further downstream of the Dhauladhar Range. Areal coverage of the steeper granite domain is ~110 km$^2$, while the moderately steep domain extends over ~460 km$^2$. In calculating the areal coverage of the moderately steep domain, we have excluded the low-slope Kangra Basin.

To evaluate the relative erosional input from the Higher Himalaya and the Lesser Himalaya in our $^{10}$Be samples from the AF1 and AF2 units, we used the calculated quartz-contribution factor (QCF; section 3.3, equations (4) and (5)). The AF2 unit has the highest QCF from the Higher Himalaya (ratio: 0.6–0.9), indicating dominant Higher Himalayan sediments, while the AF1 sediments exhibit a QCF of 0.2–0.35. A similarly low QCF of 0.2–0.3 is obtained for the strath terrace units AS1a–AS1c, indicating a higher contribution from Lesser Himalayan sediments to both AF1 and AS1a–AS1c. At the same time, erosion rates from AF1 and AS1a–AS1c differ substantially (<0.4 mm/yr versus 1–2.9 mm/yr; Table 2, Fig. 6).

### 5.5. Shifting loci of erosion

Variations in the lithological composition of our samples indicate changes in loci of erosion in the catchments over time. 'Quartz-clast corrected' paleo-erosion rates vs. the quartz-contribution factor in Fig. 6 illustrates sample variations with changing Higher Himalayan and Lesser Himalayan/Upper Siwalik sediment input. The deposits of the AF1 alluvial fill and the conglomeratic cover gravels of the strath surfaces (AS1a–AS1c) contain more components derived from the Lesser Himalaya compared to the AF2 aggradation unit (Fig. 6). The AF2 fill has therefore been fed by sediments derived from rocks exposed on the steep slopes of the Higher Himalaya. The deposits of the aggradational AF1 phase record high erosion rates of >1 mm/yr, whereas the AS1a–AS1c gravels on the strath surfaces exhibit low erosion rates of ≤0.4 mm/yr. In contrast, the present-day river-sand samples, which also

have dominant Higher Himalayan components, are characterized by lower erosion rates of 0.8−1.3 mm/yr.

Abundant rainfall and increased runoff during wetter periods affect both the moderately steep slopes of the Lesser Himalaya and the steep slopes of the Higher Himalaya. Thus, the low erosion rates of 0.1–0.4 mm/yr that characterize the low to moderate hillslopes under the weak, monsoonal conditions prevailing during the last millennium (e.g., Olen et al., 2016 and references therein) must have increased by an order of magnitude to rates between 1 and 3 mm/yr during protracted, stronger monsoons in the past. Similarly, the 'present-day' erosion rates of ~0.8–1.3 mm/yr in the steep-slope areas of the Higher Himalaya must have increased two- to threefold, reaching 2–3.5 mm/yr (Fig. 6). Such changes in erosion rates have implications for the sediment flux from the Dhauladhar Range. We used $^{10}$Be-derived erosion rates, the contributing catchment area (floodplain corrected) and, for simplicity, the bulk density of quartz ($\rho = 2650$ kg/m$^3$) to calculate the sediment flux from the moderately steep and steep compartments of the Dhauladhar Range. The estimated annual sediment contribution from the steep granite domain is ~1.1*10$^5$ m$^3$ during weak monsoon conditions and ~2.2–3.3*10$^5$ m$^3$ during strong monsoon phases – an increase by a factor of two to three. In contrast, the estimated annual sediment contribution from the moderately steep domain is ~0.46*10$^5$ m$^3$ during weak monsoon conditions, with a nearly tenfold increase to ~4.6*10$^5$ m$^3$ during stronger monsoon phases. We propose that the annual sediment flux from the steeper part of the southern flank of the Dhauladhar Range could have increased from 0.3 Mt to 0.6–0.9 Mt as a result of Late Pleistocene climate change, whereas the annual sediment flux from moderately steep areas would have increased from 0.12 Mt to 1.2 Mt. Taken together, the total annual sediment flux from the entire Dhauladhar Range could have increased fivefold from 0.45 Mt to 1.8–2.1 Mt during wetter periods. Importantly, our records of increased erosion in the Lesser Himalaya during stronger ISM conditions are furthermore supported by major changes in geochemical characteristics of sediments from the Indus Delta (Clift et al., 2008). In the absence of any evidence for major tectonic influences in our study area during the Quaternary (Thiede et al., 2017), these findings underscore the pivotal role of climate change with respect to earth-surface process rates in the Himalayan orogen.

In summary, our data show that systematic variations in erosion rates do exist on timescales spanning orbitally-driven Quaternary climate changes. Because the study area has a relatively simple tectonic setting, distinct lithologic units, and short source-to-sink travel distances, we were able to differentiate between variations in monsoonal strength, spatial shifts of areas impacted by erosion-rate changes, and variations in erosion rates on $10^3$ to $10^4$ yr timescales. In contrast, on much longer timescales and with greater sampling intervals, paleo-erosion rates from this environment may suggest sustained, steady erosion through time (Lenard et al., 2020). In the case of the Himalayan source-to-sink system, this apparent steadiness in erosion rates might ultimately be related to the homogenization of variable erosion rates in different sectors of the orogen and the buffering capability of the large Indo-Gangetic plain, involving erosion and re-transport of transiently stored sediment (e.g., Goodbred and Kuehl, 2000; Lupker et al., 2012).

## 6. Conclusions

Paleo-erosion rates from the Dhauladhar Range over the last ~120 kyr range from 0.1 to 3.4 mm/yr. By combining $^{10}$Be-derived paleo-erosion rates from sedimentary deposits, $^{10}$Be-based catchment-wide modern erosion rates, clast lithology, paleoclimatic proxies, morphometric indices, and sediment architecture,

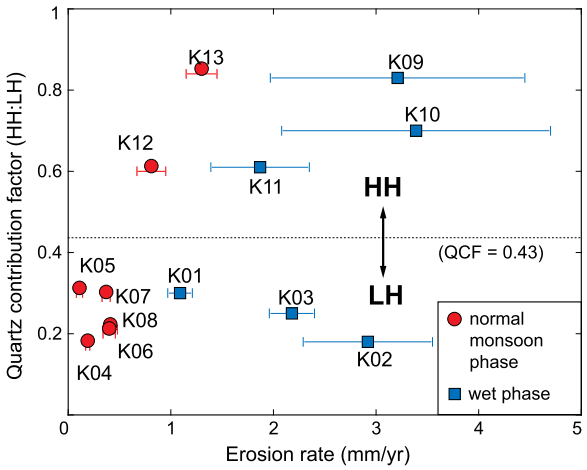


**Fig. 6.** Modern and paleo-erosion rates from Kangra Basin (calculated using LSDn model and comprising a quartz-clast and floodplain correction as described in methods section, Table 2) plotted against relative quartz-contribution factor (QCF) from the Higher Himalayan granite and the Lesser Himalayan quartzite as measured in the analyzed samples. During drier conditions, when Lesser Himalayan quartzites dominate (QCF < 0.43) in the samples, erosion rates are overall lower than the present-day river-sand samples (K12 and K13) that are primarily derived from the Higher Himalayan units (QCF > 0.43). However, during stronger, wetter monsoon periods (AF1 and AF2) the Lesser Himalayan samples (K01 to K03) exhibit a transient increase in erosion rate by an order of magnitude; similarly, Higher Himalayan erosion rates also increase 2–3 times.

we arrive at the following principal conclusions. First, sediment aggradation in the low-slope fluvial areas of the Kangra Basin likely occurred during or at the onset of wetter periods, whereas the aggraded sediments were re-incised during periods of decreased monsoon intensity, lower monsoonal variability or weaker monsoon phases.

Second, during the last millennium or during similarly weak monsoonal conditions in the past, the moderately steep hillslopes of the Lesser Himalaya eroded at 0.1–0.4 mm/yr whereas the areas of the steeper slopes of the Higher Himalaya eroded at 0.8–1.3 mm/yr, clearly documenting spatial variations in erosion.

Third, during stronger monsoon phases, especially at the transition from glacial to interglacial periods, measured paleo-erosion rates were higher for short intervals. Under these conditions, the moderate hillslopes of the Lesser Himalaya show an increase in erosion rate by one order of magnitude, whereas the steeper Higher Himalayan hillslopes increased by a factor of 2–3, exceeding 2 mm/yr. Steeper hillslopes show the highest erosion rates, but regions with moderate slopes exhibit the highest increase in erosion rates during wetter periods or during the transition to wetter conditions. Overall, the $^{10}$Be erosion rates oscillate around the Myr-timescale erosion rates of ~1.2–2 mm/yr that have been derived from thermochronology.

Fourth, based on $^{10}$Be-derived erosion rates and upstream contributing area, we predict that during climate shifts toward wetter conditions the total sediment flux from the southern flank of central Dhauladhar range may increase fivefold from ~0.4 Mt/yr to 1.8–2.1 Mt/yr.

Finally, our data support the notion that in any given steepness regime and lithology, the effects of climate change will modulate the short-term variations in erosion rates reflected by cosmogenic nuclides and other proxy indicators of erosion; in addition these short-term rates on millennial timescales can differ significantly from long-term erosion rates on geological timescales, emphasizing that the contrast in rates depends on the length of the data-integration interval.

## CRediT authorship contribution statement

Saptarshi Dey: Conceptualization, methodology, data curation, writing.
Bodo Bookhagen: Writing, reviewing, editing and data curation.
Rasmus C. Thiede: Conceptualization, writing, reviewing.
Hella Wittmann: Methodology, data curation, writing.
Naveen Chauhan: Methodology, data curation.
Vikrant Jain: Supervision.
Manfred R. Strecker: Writing, editing, reviewing, supervision.

## Declaration of competing interest

The authors declare that they have no known competing financial interests or personal relationships that could have appeared to influence the work reported in this paper.

## Acknowledgement

S. Dey is supported by IIT Gandhinagar post-doctoral fellowship (IP/IITGN/ES/SD/201718-01) and DST-INSPIRE faculty research fellowship (DST/INSPIRE/04/2017/003278). AMS measurements were funded by DFG-GRK 1364 (Deutsche Forschungsgemeinschaft) and grants to M. Strecker (STR 373/19-2) and R. Thiede (TH 1371/9-1). We thank T. Tsering and C. Singh for their assistance during fieldwork and C. Kallich for helping with improving our graphics. We also thank V. Godard for comments on an earlier draft of this manuscript. We are thankful to Douglas Burbank and the editor J. P. Avouac for their help and insightful suggestions and reviews.

## Appendix. Supplementary material

Supplementary material related to this article can be found online at https://doi.org/10.1016/j.epsl.2021.117326.

## References

Adams, B.A., Whipple, K.X., Forte, A.M., Heimsath, A.M., Hodges, K.V., 2020. Climate controls on erosion in tectonically active landscapes. Sci. Adv. 6 (42). https://doi.org/10.1126/sciadv.aaz3166.

Armitage, J.J., Duller, R.A., Whittaker, A.C., Allen, P.A., 2011. Transformation of tectonic and climatic signals from source to sedimentary archive. Nat. Geosci. 4 (4), 231–235. https://doi.org/10.1038/ngeo1087.

Bailey, R.M., Arnold, L.J., 2006. Statistical modelling of single grain quartz De distributions and an assessment of procedures for estimating burial dose. Quat. Sci. Rev. 25 (19–20), 2475–2502. https://doi.org/10.1016/j.quascirev.2005.09.012.

Balco, G., Stone, J.O., Lifton, N.A., Dunai, T.J., 2008. A complete and easily accessible means of calculating surface exposure ages or erosion rates from 10Be and 26Al measurements. Quat. Geochronol. 3 (3), 174–195. https://doi.org/10.1016/j.quageo.2007.12.001.

Blythe, A.E., Burbank, D.W., Carter, A., Schmidt, K., Putkonen, J., 2007. Plio-Quaternary exhumation history of the central Nepalese Himalaya: 1. Apatite and zircon fission track and apatite [U-Th]/He analyses. Tectonics 26 (3). https://agupubs.onlinelibrary.wiley.com/doi/full/10.1029/2006TC001990.

Bonnet, C., Malavieille, J., Mosar, J., 2007. Interactions between tectonics, erosion, and sedimentation during the recent evolution of the Alpine orogen: analogue modeling insights. Tectonics 26 (6). https://doi.org/10.1029/2006TC002048.

Bookhagen, B., Strecker, M.R., 2012. Spatiotemporal trends in erosion rates across a pronounced rainfall gradient: examples from the southern Central Andes. Earth Planet. Sci. Lett. 327, 97–110. https://doi.org/10.1016/j.epsl.2012.02.005.

Bookhagen, B., Thiede, R.C., Strecker, M.R., 2005. Abnormal monsoon years and their control on erosion and sediment flux in the high, arid northwest Himalaya. Earth Planet. Sci. Lett. 231 (1–2), 131–146. https://doi.org/10.1016/j.epsl.2004.11.014.

Borchers, B., Marrero, S., Balco, G., Caffee, M., Goehring, B., Lifton, N., Nishiizumi, K., Phillips, F., Schaefer, J., Stone, J., 2016. Geological calibration of spallation production rates in the CRONUS-Earth project. Quat. Geochronol. 31, 188–198.

Braucher, R., Merchel, S., Borgomano, J., Bourlès, D.L., 2011. Production of cosmogenic radionuclides at great depth: a multi element approach. Earth Planet. Sci. Lett. 309 (1–2), 1–9. https://doi.org/10.1016/j.epsl.2011.06.036.

Bridgland, D., Westaway, R., 2008. Climatically controlled river terrace staircases: a worldwide Quaternary phenomenon. Geomorphology 98 (3–4), 285–315. https://doi.org/10.1016/j.geomorph.2006.12.032.

Burbank, D.W., Blythe, A.E., Putkonen, J., Pratt-Sitaula, B., Gabet, E., Oskin, M., Barros, A., Ojha, T.P., 2003. Decoupling of erosion and precipitation in the Himalayas. Nature 426 (6967), 652–655. https://doi.org/10.1038/nature02187.

Charreau, J., Blard, P.H., Puchol, N., Avouac, J.P., Lallier-Vergès, E., Bourlès, D., Braucher, R., Gallaud, A., Finkel, R., Jolivet, M., Chen, Y., 2011. Paleo-erosion rates in Central Asia since 9 Ma: a transient increase at the onset of Quaternary glaciations? Earth Planet. Sci. Lett. 304 (1–2), 85–92. https://doi.org/10.1016/j.epsl.2011.01.018.

Cheng, H., Edwards, R.L., Sinha, A., Spötl, C., Yi, L., Chen, S., Kelly, M., Kathayat, G., Wang, X., Li, X., Kong, X., 2016. The Asian monsoon over the past 640,000 years and ice age terminations. Nature 534 (7609), 640–646. https://doi.org/10.1038/nature18591.

Chmeleff, J., von Blanckenburg, F., Kossert, K., Jakob, D., 2010. Determination of the 10Be half-life by multicollector ICP-MS and liquid scintillation counting. Nucl. Instrum. Methods Phys. Res., Sect. B, Beam Interact. Mater. Atoms 268 (2), 192–199.

Clift, P.D., Giosan, L., Blusztajn, J., Campbell, I.H., Allen, C., Pringle, M., Tabrez, A.R., Danish, M., Rabbani, M.M., Alizai, A., Carter, A., 2008. Holocene erosion of the Lesser Himalaya triggered by intensified summer monsoon. Geology 36 (1), 79–82. https://doi.org/10.1130/G24315A.1.

DeCelles, P.G., Robinson, D.M., Quade, J., Ojha, T.P., Garzione, C.N., Copeland, P., Upreti, B.N., 2001. Stratigraphy, structure, and tectonic evolution of the Himalayan fold-thrust belt in western Nepal. Tectonics 20 (4), 487–509. https://doi.org/10.1029/2000TC001226.

Deeken, A., Thiede, R.C., Sobel, E.R., Hourigan, J.K., Strecker, M.R., 2011. Exhumational variability within the Himalaya of northwest India. Earth Planet. Sci. Lett. 305 (1–2), 103–114. https://doi.org/10.1016/j.epsl.2011.02.045.

Demenocal, P., Ortiz, J., Guilderson, T., Adkins, J., Sarnthein, M., Baker, L., Yarusinsky, M., 2000. Abrupt onset and termination of the African Humid Period: rapid climate responses to gradual insolation forcing. Quat. Sci. Rev. 19 (1–5), 347–361. https://doi.org/10.1016/S0277-3791(99)00081-5.

Dewald, A., Heinze, S., Jolie, J., Zilges, A., Dunai, T., Rethemeyer, J., Melles, M., Staubwasser, M., Kuczewski, B., Richter, J., Radtke, U., 2013. CologneAMS, a dedicated center for accelerator mass spectrometry in Germany. Nucl. Instrum. Methods Phys. Res., Sect. B, Beam Interact. Mater. Atoms 294, 18–23. https://doi.org/10.1016/j.nimb.2012.04.030.

Dey, S., Thiede, R.C., Schildgen, T.F., Wittmann, H., Bookhagen, B., Scherler, D., Jain, V., Strecker, M.R., 2016. Climate-driven sediment aggradation and incision since the late Pleistocene in the NW Himalaya, India. Earth Planet. Sci. Lett. 449, 321–331. https://doi.org/10.1016/j.epsl.2016.05.050.

Dunai, T.J., 2010. Cosmogenic Nuclides: Principles, Concepts and Applications in the Earth Surface Sciences. Cambridge University Press.

Fuchs, G., 1975. Contributions to the Geology of the North-Western Himalayas. Geologische Bundesanstalt.

Garcin, Y., Schildgen, T.F., Acosta, V.T., Melnick, D., Guillemoteau, J., Willenbring, J., Strecker, M.R., 2017. Short-lived increase in erosion during the African Humid Period: evidence from the northern Kenya Rift. Earth Planet. Sci. Lett. 459, 58–69. https://doi.org/10.1016/j.epsl.2016.11.017.

Godard, V., Bourlès, D.L., Spinabella, F., Burbank, D.W., Bookhagen, B., Fisher, G.B., Moulin, A., Lèanni, L., 2014. Dominance of tectonics over climate in Himalayan denudation. Geology 42 (3), 243–246.

Godard, V., Maheo, G., Mukherjee, S., Sterb, M., Maleappane, E., Leloup, H., ASTER Team, 2018. Rapid denudation at the Dhauladhar range front, Himachal Pradesh, India. In: 33rd Himalaya Karakoram Tibet Workshop Abstract Volume, p. 56.

Goodbred Jr., S.L., Kuehl, S.A., 2000. Enormous Ganges-Brahmaputra sediment discharge during strengthened early Holocene monsoon. Geology 28 (12), 1083–1086. https://doi.org/10.1130/0091-7613(2000)28<1083:EGSDDS>2.0.CO;2.

Hidy, A.J., Gosse, J.C., Pederson, J.L., Mattern, J.P., Finkel, R.C., 2010. A geologically constrained Monte Carlo approach to modeling exposure ages from profiles of cosmogenic nuclides: an example from Lees Ferry, Arizona. Geochem. Geophys. Geosyst. 11 (9).

Huybers, P., 2006. Early Pleistocene glacial cycles and the integrated summer insolation forcing. Science 313 (5786), 508–511. https://doi.org/10.1126/science.1125249.

Jaiswal, M., Srivastava, P., Tripathi, J., Islam, R., 2008. Feasibility of the SAR technique on quartz sand of terraces of NW Himalaya: a case study from Devprayag. Geochronometria 31 (1), 45–52.

Kapannusch, R., Scherler, D., King, G., Wittmann, H., 2020. Glacial influence on late Pleistocene 10Be-derived paleo-erosion rates in the north-western Himalaya, India. Earth Planet. Sci. Lett. 547, 116441. https://doi.org/10.1016/j.epsl.2020.116441.

Kirby, E., Whipple, K.X., 2012. Expression of active tectonics in erosional landscapes. J. Struct. Geol. 44, 54–75. https://doi.org/10.1016/j.jsg.2012.07.009.

Lague, D., 2014. The stream power river incision model: evidence, theory and beyond. Earth Surf. Process. Landf. 39 (1), 38–61. https://doi.org/10.1002/esp.3462.

Lal, D., 1991. Cosmic ray labeling of erosion surfaces: in situ nuclide production rates and erosion models. Earth Planet. Sci. Lett. 104 (2–4), 424–439.

Lenard, S.J., Lavé, J., France-Lanord, C., Aumaître, G., Bourlès, D.L., Keddadouche, K., 2020. Steady erosion rates in the Himalayas through late Cenozoic climatic changes. Nat. Geosci. 1–5. https://doi.org/10.1038/s41561-020-0585-2.

Lifton, N., Sato, T., Dunai, T.J., 2014. Scaling in situ cosmogenic nuclide production rates using analytical approximations to atmospheric cosmic-ray fluxes. Earth Planet. Sci. Lett. 386, 149–160. https://doi.org/10.1016/j.epsl.2013.10.052.

Lupker, M., Blard, P.H., Lave, J., France-Lanord, C., Leanni, L., Puchol, N., Charreau, J., Bourlès, D., 2012. 10Be-derived Himalayan denudation rates and sediment budgets in the Ganga basin. Earth Planet. Sci. Lett. 333, 146–156. https://doi.org/10.1016/j.gca.2012.02.001.

Mandal, S.K., Scherler, D., Wittmann, H., 2021. Tectonic accretion controls erosional cyclicity in the Himalaya. AGU Adv. 2 (3). https://doi.org/10.1029/2021AV000487.

Murray, A.S., Wintle, A.G., 2003. The single aliquot regenerative dose protocol: potential for improvements in reliability. Radiat. Meas. 37 (4–5), 377–381. https://doi.org/10.1016/S1350-4487(03)00053-2.

Olen, S.M., Bookhagen, B., Strecker, M.R., 2016. Role of climate and vegetation density in modulating denudation rates in the Himalaya. Earth Planet. Sci. Lett. 445, 57–67. https://doi.org/10.1016/j.epsl.2016.03.047.

Pratt, B., Burbank, D.W., Heimsath, A., Ojha, T., 2002. Impulsive alluviation during early Holocene strengthened monsoons, central Nepal Himalaya. Geology 30 (10), 911–914. https://doi.org/10.1130/0091-7613(2002)030<0911:IADEHS>2.0.CO;2.

Preusser, F., 2003. IRSL dating of K-rich feldspars using the SAR protocol: comparison with independent age control. Ancient TL 21 (1), 17–23.

Repasch, M., Karlstrom, K., Heizler, M., Pecha, M., 2017. Birth and evolution of the Rio Grande fluvial system in the past 8 Ma: progressive downward integration and the influence of tectonics, volcanism, and climate. Earth-Sci. Rev. 168, 113–164. https://doi.org/10.1016/j.earscirev.2017.03.003.

Roberts, H.M., 2007. Assessing the effectiveness of the double-SAR protocol in isolating a luminescence signal dominated by quartz. Radiat. Meas. 42 (10), 1627–1636. https://doi.org/10.1016/j.radmeas.2007.09.010.

Scherler, D., Bookhagen, B., Wulf, H., Preusser, F., Strecker, M.R., 2015. Increased late Pleistocene erosion rates during fluvial aggradation in the Garhwal Himalaya, northern India. Earth Planet. Sci. Lett. 428, 255–266. https://doi.org/10.1016/j.epsl.2015.06.034.

Schwanghart, W., Scherler, D., 2014. TopoToolbox 2–MATLAB-based software for topographic analysis and modeling in Earth surface sciences. Earth Surf. Dyn. 2 (1), 1–7. https://doi.org/10.5194/esurf-2-1-2014.

Srivastava, P., Misra, D.K., 2012. Optically stimulated luminescence chronology of terrace sediments of Siang River, Higher NE Himalaya: comparison of Quartz and Feldspar chronometers. J. Geol. Soc. India 79 (3), 252–258. https://doi.org/10.1007/s12594-012-0043-x.

Srivastava, P., Rajak, M.K., Singh, L.P., 2009. Late Quaternary alluvial fans and paleosols of the Kangra basin, NW Himalaya: tectonic and paleoclimatic implications. Catena 76 (2), 135–154. https://doi.org/10.1016/j.catena.2008.10.004.

Steck, A., 2003. Geology of the NW Indian Himalaya. Eclogae Geol. Helv. 96, 147–196.

Stone, J.O., 2000. Air pressure and cosmogenic isotope production. J. Geophys. Res., Solid Earth 105 (B10), 23753–23759.

Thakur, V.C., Joshi, M., Sahoo, D., Suresh, N., Jayangondapermal, R., Singh, A., 2014. Partitioning of convergence in Northwest Sub-Himalaya: estimation of late Quaternary uplift and convergence rates across the Kangra reentrant, North India. Int. J. Earth Sci. 103 (4), 1037–1056. https://doi.org/10.1007/s00531-014-1016-7.

Thiede, R.C., Ehlers, T.A., 2013. Large spatial and temporal variations in Himalayan denudation. Earth Planet. Sci. Lett. 371, 278–293. https://doi.org/10.1016/j.epsl.2013.03.004.

Thiede, R., Robert, X., Stübner, K., Dey, S., Faruhn, J., 2017. Sustained out-of-sequence shortening along a tectonically active segment of the Main Boundary thrust: the Dhauladhar Range in the northwestern Himalaya. Lithosphere 9 (5), 715–725. https://doi.org/10.1130/L630.1.

Thompson, J.A., Chen, J., Yang, H., Li, T., Bookhagen, B., Burbank, D., 2018. Coarse- versus fine-grain quartz OSL and cosmogenic 10Be dating of deformed fluvial terraces on the northeast Pamir margin, northwest China. Quat. Geochronol. 46, 1–15. https://doi.org/10.1016/j.quageo.2018.01.002.

Tofelde, S., Schildgen, T.F., Savi, S., Pingel, H., Wickert, A.D., Bookhagen, B., Wittmann, H., Alonso, R.N., Cottle, J., Strecker, M.R., 2017. 100 kyr fluvial cut-and-fill terrace cycles since the Middle Pleistocene in the southern Central Andes, NW Argentina. Earth Planet. Sci. Lett. 473, 141–153. https://doi.org/10.1016/j.epsl.2017.06.001.

Vance, D., Bickle, M., Ivy-Ochs, S., Kubik, P.W., 2003. Erosion and exhumation in the Himalaya from cosmogenic isotope inventories of river sediments. Earth Planet. Sci. Lett. 206 (3–4), 273–288. https://doi.org/10.1016/S0012-821X(02)01102-0.

Von Blanckenburg, F., 2005. The control mechanisms of erosion and weathering at basin scale from cosmogenic nuclides in river sediment. Earth Planet. Sci. Lett. 237 (3–4), 462–479.

Wegmann, K.W., Pazzaglia, F.J., 2009. Late Quaternary fluvial terraces of the Romagna and Marche Apennines, Italy: climatic, lithologic, and tectonic controls on terrace genesis in an active orogen. Quat. Sci. Rev. 28 (1–2), 137–165. https://doi.org/10.1016/j.quascirev.2008.10.006.

Weldeab, S., Rühlemann, C., Bookhagen, B., Pausata, F.S., Perez-Lua, F.M., 2019. Enhanced Himalayan glacial melting during YD and H1 recorded in the northern Bay of Bengal. Geochem. Geophys. Geosyst. 20 (5), 2449–2461. https://doi.org/10.1029/2018GC008065.

Wittmann, H., von Blanckenburg, F., Guyot, J.L., Maurice, L., Kubik, P.W., 2009. From source to sink: preserving the cosmogenic 10Be-derived denudation rate signal of the Bolivian Andes in sediment of the Beni and Mamoré foreland basins. Earth Planet. Sci. Lett. 288 (3–4), 463–474. https://doi.org/10.1016/j.epsl.2009.10.008.

Wulf, H., Bookhagen, B., Scherler, D., 2010. Seasonal precipitation gradients and their impact on fluvial sediment flux in the Northwest Himalaya. Geomorphology 118 (1–2), 13–21. https://doi.org/10.1016/j.geomorph.2009.12.003.